Communications in Theoretical Physics

Commun. Theor. Phys. **77** (2025) 075301 (12pp) https://doi.org/10.1088/1572-9494/ada884
CSTR: 32041.14.CTP.ada884

The boundary effect of QGP droplets and the self-similarity effect of hadrons on QGP–hadron phase transition

Tingting Dai[1], Huiqiang Ding[1], Luan Cheng[1,2], Weining Zhang[1] and Enke Wang[2]

[1] School of Physics, Dalian University of Technology, Dalian 116024, China
[2] Institute of Quantum Matter, South China Normal University, Guangzhou 510631, China

E-mail: luancheng@dlut.edu.cn

Received 25 September 2024, revised 3 January 2025
Accepted for publication 10 January 2025
Published 27 March 2025

Abstract

We investigate the boundary effect of quark–gluon plasma (QGP) droplets and the self-similarity effect of hadrons on QGP–hadron phase transition. In intermediate- or low-energy collisions, when the transverse momentum is below quantum chromodynamics (QCD) scale, QGP cannot be produced. However, if the transverse momentum changes to a relatively large value, a small-scale QGP droplet is produced. The modified MIT bag model with the multiple reflection expansion method is employed to study the QGP droplet with the curved boundary effect. It is found that the energy density, entropy density and pressure of QGP with the influence are smaller than those without the influence. In the hadron phase, we propose the two-body fractal model (TBFM) to study the self-similarity structure, arising from resonance, quantum correlation and interaction effects. It is observed that the energy density, entropy density and pressure increase due to the self-similarity structure. We calculate the transverse momentum spectra of pions with the self-similarity structure influence, which show good agreement with experimental data. Considering both boundary effect and self-similarity structure influence, our model predicts an increase in the transition temperature compared to the scenarios without these two effects in the High Intensity heavy-ion Accelerator Facility (HIAF) energy region, 2.2 GeV to approximately 4.5 GeV.

Keywords: QGP droplet, multiple reflection expansion method, self-similarity structure, phase transition

(Some figures may appear in colour only in the online journal)

1. Introduction

Quantum chromodynamics (QCD) theory predicts that quark–gluon plasma (QGP) can be formed after the de-confinement of quarks and gluons [1–3]. In recent years, the production of QGP has been discovered in heavy-ion collisions [4–6]. To gain a clearer understanding of the properties of QGP, besides studying its properties, it is also significant to study QCD phase structure and the QCD critical point [7–9]. The QCD phase diagram is an important tool to explore QCD phase structure and the critical point. Previous studies focused on exploring the phase diagram in the region of low chemical potential [8, 10]. However, recent results from BES-II experiments indicate that the critical point may not exist in high-energy collisions with a chemical potential $\mu_B < 450$ MeV [11]. Consequently, it is significant to investigate the QCD critical point and the phase transition in mid-energy collisions with a high chemical potential. To date, mid-energy experimental programs Beam Energy Scan Phase I (BES-I) and Beam Energy Scan Phase II (BES-II) at Relativistic Heavy Ion Collider (RHIC) have been run successfully, and low- and mid-energy facilities like High Intensity heavy-ion Accelerator Facility (HIAF), Facility for Antiproton and Ion Research (FAIR) and Nuclotron-based Ion Collider Facility

(NICA) have been proposed and are planned to run in the near future [12, 13].

Previous studies concentrated on the phase structure in the thermodynamic limit [14–16]. In conditions of high temperature or large baryon density, the production of large-scale QGP [6, 17–20] can be approximately described in the thermodynamic limit [21]. However, in mid-energy collisions, where the baryon density is not large enough and the transverse momentum transfer fluctuates to a momentum less than QCD Λ scale, QGP cannot be produced and only hadrons can be produced. In the region where the transverse momentum transfer to the momentum which is higher than QCD Λ scale [22], a small-scale QGP droplet can be produced [23–25]. The curved boundary of these small-scale QGP droplets results in one side being QGP and the other side being hadron matter, inducing surface tension due to different densities [26, 27]. Hence, the thermodynamic limit cannot be used in this scenario, and the effects of curved boundary and surface tension should be considered. In this paper, we study the boundary effect on small-scale QGP and QGP–hadron transition. After the phase transition, in the hadron phase, the collective flow, an important phenomenon observed in experiments [28, 29], results in the co-movement of the π meson and its neighboring π meson. This will induce resonance [30, 31] in pion gas. The π–π resonance effect for pion gas will also be considered in our study.

In this paper, we study QGP–hadron phase transition considering two influences: the surface tension and boundary effect for QGP droplets, and the π–π resonance in pion gas. For QGP droplets, the modified MIT bag model, extended by the multiple reflection expansion (MRE) method [32], is employed to describe the droplet with curvature and surface tension at the boundary. For pion gas, we propose the two-body fractal model (TBFM) [33] to analyze the resonance influence on pion gas near the critical temperature. Finally, we explore QGP–hadron phase transition under the influences of surface tension and resonance, and compare the results with and without these influences, demonstrating the significant effects of surface tension and resonance on the phase transition.

2. Model and method

2.1. The boundary effect of a QGP droplet

Under conditions of high temperature or large baryon density, a large number of quarks and gluons are produced, leading to the formation of large-scale QGP [34]. However, in mid-energy collisions [35–37], where the temperature and density are not large enough, and the transverse momentum [38, 39] fluctuates to a small value less than QCD Λ scale, free quarks and gluons cannot be produced and, instead, hadrons are produced. Only in the region where the transverse momentum fluctuates to a large value larger than QCD Λ scale can the small-scale QGP—QGP droplet [23, 24] be produced. Consequently, for the QGP droplet, one side of the curved boundary is QGP, while the other side is hadrons. This will induce surface tension. The effects of the curved boundary and the surface tension need to be considered.

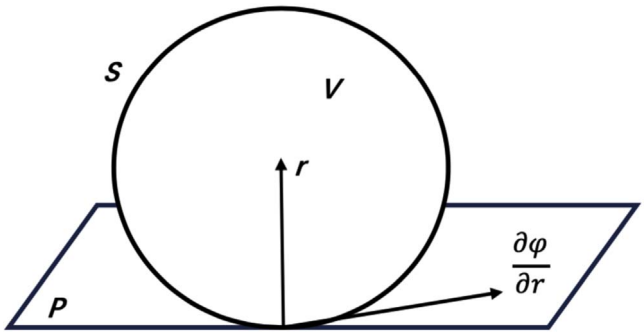

Figure 1. Potential field of QGP droplet.

The MIT bag model is an effective model to describe the thermodynamics of quarks and gluons confined in a bag [40]. The MRE method is an important approach to study the finite size effect of a system with a curved boundary in powers of the system radius [27, 32, 41]. It can be used to analyze the influence of a curved boundary. In Madsen's work [42, 43], the MRE method was used to investigate the effect of curvature caused by massive s quark in a finite size MIT bag model. Here, in our study, we apply the MRE method to investigate the curvature of the boundary and the surface tension of a small-scale QGP droplet produced in mid-energy collisions.

We treat the QGP droplet as a source field φ, the radius of a QGP droplet points to the droplet's center.

The potential field distribution obeys the equation [44]

$$\Delta\varphi + E\varphi = 0. \tag{1}$$

$\frac{\partial\varphi}{\partial r}$, recognized as the surface tension, is along the tangent plane P of the point on surface S as shown in figure 1.

In the thermodynamic limit, the density of microstates with momentum between k and $k + dk$ is

$$\rho(k)\mathrm{d}k \sim \frac{Vk^2}{2\pi^2}\mathrm{d}k. \tag{2}$$

However, a correction for the density of microstates due to the boundary effect in a small-scale QGP droplet needs to be considered. The correction can be calculated using MRE for Green's function method.

The MRE for a time-independent Green's function has the following form:

$$\begin{aligned} S(\boldsymbol{r},\boldsymbol{r}') = {} & S^{(0)}(\boldsymbol{r},\boldsymbol{r}') + \oint_{\partial\Omega}\mathrm{d}\sigma_\alpha S^{(0)}(\boldsymbol{r},\boldsymbol{\alpha})K(\boldsymbol{\alpha})S^{(0)}(\boldsymbol{\alpha},\boldsymbol{r}') \\ & + \oint_{\partial\Omega}\mathrm{d}\sigma_\alpha\mathrm{d}\sigma_\beta S^{(0)}(\boldsymbol{r},\boldsymbol{\alpha})K(\boldsymbol{\alpha})S^{(0)}(\boldsymbol{\alpha},\boldsymbol{\beta})K(\boldsymbol{\beta})S^{(0)}(\boldsymbol{\beta},\boldsymbol{r}') \\ & + \cdots . \end{aligned} \tag{3}$$

Here, $S^{(0)}$ corresponds to the free field satisfying $(\mathrm{i}\gamma^\mu\partial_\mu - m)S^{(0)}(x - x') = \delta(x - x')$. Ω is the finite space of the QGP droplet. K is the reflection kernel in the integral over surface $\partial\Omega$ and describes the boundary effect using corrections of increasing order in the principal radii of curvature as $\left(\frac{1}{R_1} + \frac{1}{R_2}\right)^n$, $n = 0, 1, \ldots$. Here, R_1 and R_2 are the principal radii of curvature, $R_1 = R_2 = R$. $\boldsymbol{r}$ and $\boldsymbol{r}'$ represent the spatial vectors in Ω. $\boldsymbol{\alpha}$ and $\boldsymbol{\beta}$ are the spatial vectors on $\partial\Omega$.

Based on the relation [32] of the density of microstates $\rho(\omega)$ and S matrix,

$$\rho(\omega) = \mp\frac{1}{\pi}\,\mathrm{Im}\int_{\Omega} \mathrm{d}^3\boldsymbol{r}\,\mathrm{tr}[S(\boldsymbol{r}, \boldsymbol{r}', \omega \pm \mathrm{i}\varepsilon)\gamma^0]. \tag{4}$$

Considering the reflection of order $n = 0,\ 1$ in equation (3) and performing the trace operation through equation (4), we can obtain the MRE of density of states in powers of $\frac{1}{kR}$, where R is the radius of the QGP droplet:

$$\begin{aligned}\rho(k) &= \tfrac{Vk^2}{2\pi^2}\left[1 + 6\pi^2 f_S\left(\tfrac{m}{k}\right)\tfrac{1}{(kR)} + 12\pi^2 f_C\left(\tfrac{m}{k}\right)\tfrac{1}{(kR)^2} + \ldots\right] \\ &= \tfrac{Vk^2}{2\pi^2} + f_S\left(\tfrac{m}{k}\right)kA + f_C\left(\tfrac{m}{k}\right)C + \ldots\end{aligned} \tag{5}$$

The detailed derivations can be found in [45]. The second term in equation (5) corresponds to the $n = 0$ order for boundary curvature correction. Integrating the kernel K over the surface, A can be derived as the surface area of a QGP droplet, $A = 4\pi R^2$. The third term in equation (5) arises from the curvature of the boundary with $n = 1$ order, where C represents the extrinsic curvature given by the surface integral $C = \oint_{\partial\Omega} \mathrm{d}^2\sigma(\frac{1}{R_1(\sigma)} + \frac{1}{R_2(\sigma)}) = 8\pi R$. Considering different corrections of orders $n = 0,\ 1$ in the principal radii of curvature within the second term of the Green's function equation (3), f_S and f_C are derived as

$$f_S = -\frac{1}{8\pi}\left[1 - \frac{2}{\pi}\arctan\left(\frac{k}{m}\right)\right], \tag{6}$$

$$f_C = \frac{1}{12\pi^2}\left\{1 - \frac{3k}{2m}\left[\frac{\pi}{2} - \arctan\left(\frac{k}{m}\right)\right]\right\}. \tag{7}$$

Taking surface tension and curvature of a QGP droplet into account, the density of microstates for quarks and anti-quarks with momentum p_q is obtained from equation (5) as

$$\rho_{qMRE} = \rho_{\bar{q}MRE} = g_q V p_q^2\left[\frac{1}{2\pi^2} + \frac{3}{p_q R}f_S + \frac{6p_q^2}{(p_q R)^2}f_C\right]. \tag{8}$$

For gluons with mass $m = 0$, it follows that $f_s = 0$ and $f_C = -\frac{1}{6\pi^2}$. The density of microstates is

$$\rho_{gMRE} = g_g\left(\frac{Vp_g^2}{2\pi^2} - \frac{V}{\pi^2 R^2}\right), \tag{9}$$

where p_g is the momentum of gluons. g_q and g_g denote the degeneracy factor of quarks (anti-quarks) and gluons.

Applying the density of microstates under the influence of surface tension and curvature above, the energy density, entropy density and pressure of a QGP droplet are expressed as

$$\begin{aligned}u_{QGP} = &\frac{1}{V}\int_0^\infty \rho_{qMRE} f_q \varepsilon_q\,\mathrm{d}p_q + \frac{1}{V}\int_0^\infty \rho_{\bar{q}MRE} f_{\bar{q}} \varepsilon_{\bar{q}}\,\mathrm{d}p_q \\ &+ \frac{1}{V}\int_0^\infty \rho_{gMRE} f_g \varepsilon_g\,\mathrm{d}p_q,\end{aligned} \tag{10}$$

$$\begin{aligned}s_{QGP} = &-\frac{1}{V}\int_0^\infty \rho_{qMRE}[f_q\,\mathrm{ln}f_q - (1+f_q)\mathrm{ln}(1+f_q)]\,\mathrm{d}p_q \\ &- \frac{1}{V}\int_0^\infty \rho_{\bar{q}MRE}[f_{\bar{q}}\,\mathrm{ln}f_{\bar{q}} \\ &- (1+f_{\bar{q}})\mathrm{ln}(1+f_{\bar{q}})]\,\mathrm{d}p_q \\ &- \frac{1}{V}\int_0^\infty \rho_{gMRE} f_g[f_g\,\mathrm{ln}f_g - (1+f_g)\mathrm{ln}(1+f_g)]\,\mathrm{d}p_g,\end{aligned} \tag{11}$$

$$\begin{aligned}P_{QGP} = &-\frac{\partial(\int_0^\infty f_q\,\rho_{qMRE}\varepsilon_q\,\mathrm{d}p_q)}{\partial V} - \frac{\partial(\int_0^\infty f_{\bar{q}}\,\rho_{\bar{q}MRE}\varepsilon_{\bar{q}}\,\mathrm{d}p_q)}{\partial V} \\ &- \frac{\partial(\int_0^\infty f_g\,\rho_{gMRE}\varepsilon_g\,\mathrm{d}p_g)}{\partial V} - B(T,\,\mu),\end{aligned} \tag{12}$$

where $\varepsilon_{q(\bar{q})}$, ε_g are the energy of quarks (anti-quarks) and gluons, where $\varepsilon_q = \varepsilon_{\bar{q}} = \sqrt{m^2 + p^2}$ and $\varepsilon_g = p_g$. $f_q, f_{\bar{q}}$ denote the Fermi distribution for quarks and anti-quarks $f_q = f_{\bar{q}}$ and f_g is the Bose distribution of gluons. The three terms in equation (12) correspond to quark, anti-quark and gluon, respectively. $B(T,\,\mu)$ is the bag pressure as a function of temperature T and chemical potential μ in the MIT bag model [46, 47]. To investigate the boundary effect, we adjust the parameters to align with recent results of lattice QCD [48, 49], obtaining the bag pressure $B(T,\,\mu)$ as

$$B(T,\,\mu) = B_0 - \left(\frac{\mu^4}{85\pi^2} + \frac{1}{4}T^2\mu^2 + \frac{1}{10}\pi^2 T^4\right), \tag{13}$$

where $B_0^{1/4} = 233.5$ MeV.

The energy density, entropy density and pressure of QGP droplets with and without the boundary effect as functions of temperature at fixed radii, $r = 1,\ 1.5,\ 7$ fm, are depicted in figure 2. The energy density, entropy density and pressure increase with temperature as shown in figures 2(a)(1), (b)(1) and (c)(1), respectively. For the sake of analysis, we compare the energy density, entropy density and pressure with (red trace) and without (blue trace) the boundary effect at fixed QGP radius $r = 1$ fm in figures 2(a), (b) and (c). At a smaller radius $r = 1$ fm, it is found that the values of three physical properties under the influence of the boundary effect are less than those without the influence. We also compare the energy density, entropy density and pressure with (red trace) and without (blue trace) the boundary effect at a fixed QGP radius $r = 7$ fm as shown in figures 2(a)(3), (b)(3) and (c)(3), respectively. The values of the three physical properties with and without boundary effect are approximately unchanged, suggesting that the influence of the boundary effect is dependent on QGP size: when the size increases, the influence decreases.

In summary, the surface tension originating from the finite size effect of small-scale QGP droplets impacts on the thermodynamics of QGP droplets, especially in mid- and low-energy collisions where small QGP droplets can be produced.

2.2. Two-body structure in pion gas

2.2.1. Two-body fractal model. The collective flow is a significant phenomenon in collision experiments. Due to the

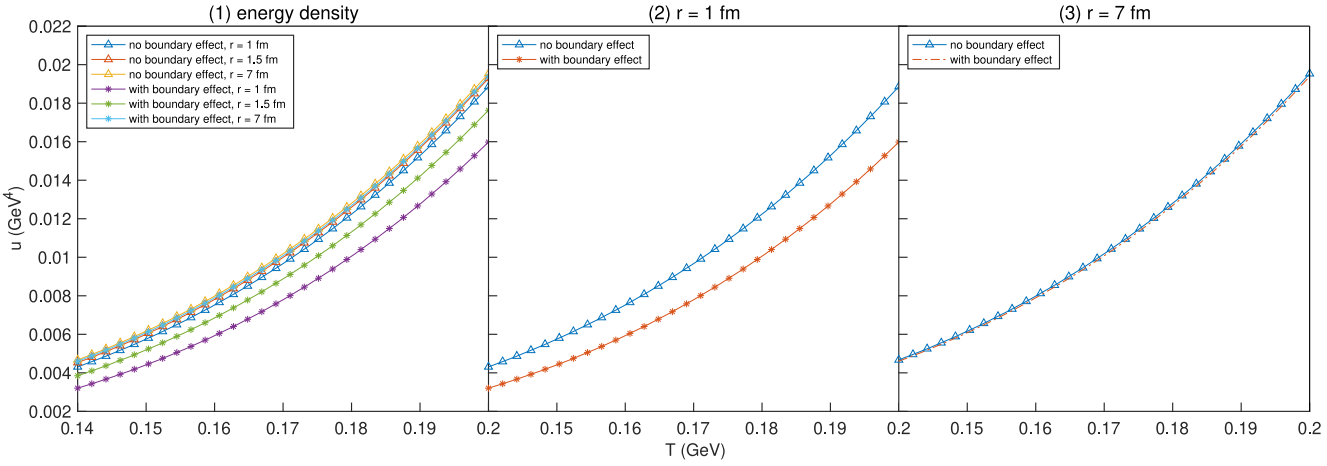

(a) Energy density

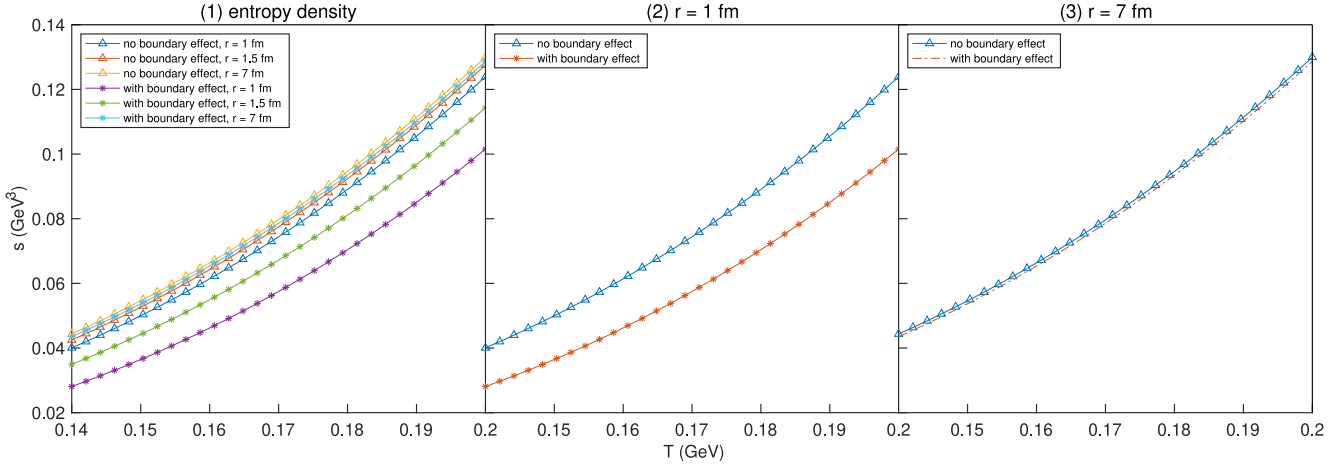

(b) Entropy density

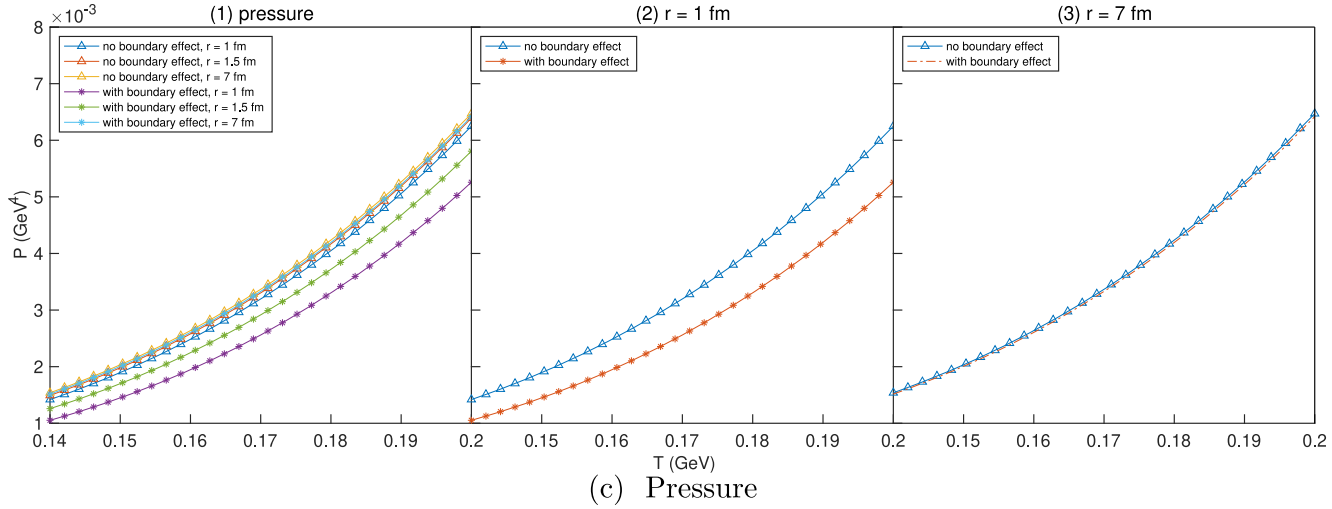

(c) Pressure

Figure 2. Thermodynamic quantities of QGP droplets with different radii, $r = 1$, 1.5, 7 fm.

collective flow, π mesons have similar momentum and frequency with their neighbors, resulting in co-movement of neighboring π mesons. Furthermore, the same frequency of neighboring π mesons will surely induce resonance [50]. Secondly, in high-energy collisions, the pion density at the phase transition temperature is approximately $\frac{N}{V} = 0.5\,\mathrm{fm}^{-3}$, and the distance between the neighboring pions is approximately $\left(\frac{V}{N}\right)^{1/3} \approx 1.3\,\mathrm{fm}$, which is less than the thermal length of a π meson, $\lambda_T = \frac{h}{\sqrt{2\pi mkT}} = 3.008\,\mathrm{fm}$. This implies the quantum correlation between two neighboring π mesons. In mid- or low-energy collisions

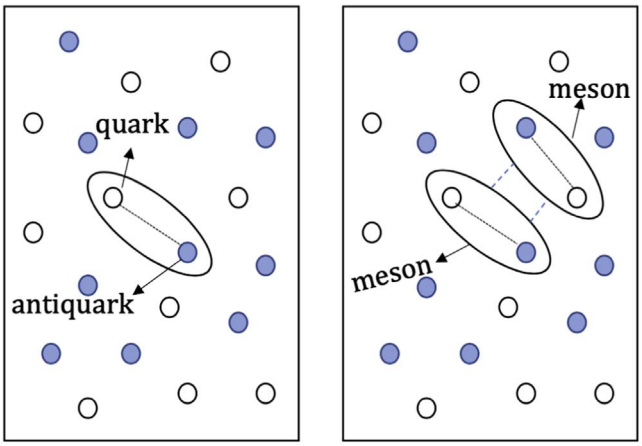

(a) quark aspect (b) meson aspect

Figure 3. Self-similarity structure of a meson and a resonant state.

with larger chemical potential and larger baryon density, the distance between the neighboring mesons is less than in high-energy collisions. Thus, the quantum correlation is larger than that of the high-energy case. Thirdly, the solution to the two-body Dirac equation (TBDE) for $u\bar{d}$ quarks [51] suggests that within a distance less than $l = 1.2$fm, a u quark has a strong interaction with a $\bar{d}$ quark. Meanwhile, the interaction distance and the pion average distance satisfy $\left(\frac{V}{N}\right)^{1/3} < 2l$, illustrating the strong interaction between a π meson and its nearest neighbor. Overall, under the influence of resonance, quantum correlation and strong interaction in a high baryon density region, a π meson and its nearest neighbor can form the two-body π–π system as depicted in figure 3(b).

Analogous to the π–π resonate state as a two-body structure, a π meson is also recognized as a two-quark bound state as shown in figure 3(a). Owing to the two-body structure, we postulate that the two-quark system and two-meson system exhibit self-similarity and apply the fractal theory to describe the characteristic. The concept of a fractal was originally proposed by Mandelbort [52, 53] to describe the similarity between the components of a structure and the structure as a whole. Tsallis statistics, inspired by the fractal theory, has been widely applied to study systems characterized by self-similarity fractal structures [54–56] in different scales. Hence, we propose the two-body fractal model (TBFM) [33], which is based on fractal-inspired Tsallis statistics to analyze a π meson and π–π bound state as the self-similarity structure in pion gas.

2.2.2. Pion gas influenced by self-similarity structures. First, from a meson aspect, we study the π meson as a two-quark bound state. The π meson is influenced by the self-similarity structure from resonance, quantum correlation and strong interaction. We introduce the modification factor q_1 to denote the self-similarity structure influence on the π meson. In the rest frame, the probability of a π meson is

$$P_{\pi 1} = \frac{\langle\psi_0|[1 + (q_1 - 1)\beta\hat{H}]^{\frac{q_1}{1-q_1}}|\psi_0\rangle}{\sum_i \langle\psi_i|[1 + (q_1 - 1)\beta\hat{H}]^{\frac{q_1}{1-q_1}}|\psi_i\rangle}, \tag{14}$$

in which β is the inverse of temperature, $\beta = 1/T$. ψ_0 is the wavefunction of a π meson, which is the ground state of the $u\bar{d}$ bound state, and ψ_i is that of $u\bar{d}$ bound states in different eigenstates. The Hamiltonian of $u\bar{d}$ bound states is

$$\hat{H} = \sqrt{m_q^2 + \boldsymbol{p}_1^2} + \sqrt{m_q^2 + \boldsymbol{p}_2^2} + \hat{V}(r), \tag{15}$$

where $\sqrt{m_q^2 + \boldsymbol{p}_{1(2)}^2}$ is the kinetic energy of u, $\bar{d}$ quarks, and $m_q = 55$MeV is the corresponding mass. $\hat{V}(r)$ is the quark potential. Here, we consider the quark potential $V(r)$ from the work of calculating the TBDE by the Crater group [51] as

$$V(r) = \frac{8\pi\Lambda^2 r}{27} - \frac{16\pi}{27r\ln[(K\mathrm{e}^2 + B_1/(\Lambda r)^2]}, \tag{16}$$

where $\Lambda = 0.4218$ GeV is the scale size, $K = 4.198$ and $B_1 = 0.05081$ are the variable parameters and e is Euler's constant.

The denominator in equation (14) represents the partition function, which is the sum of probability in all microstates:

$$\begin{aligned}
&\sum_i \langle\psi_i|[1 + (q_1 - 1)\beta\hat{H}]^{\frac{q_1}{1-q_1}}|\psi_i\rangle \\
&= [1 + (q_1 - 1)\beta E_\pi]^{\frac{q_1}{1-q_1}} + [1 + (q_1 - 1)\beta E_\rho]^{\frac{q_1}{1-q_1}} \\
&\quad + \frac{V}{(2\pi)^6}\int_{p_{\min}}^{\infty}\int_{r_{\min}}^{r_{\max}} [1 + (q_1 - 1)\beta \\
&\quad \times (\sqrt{m_q^2 + \boldsymbol{p}_1^2} + \sqrt{m_q^2 + \boldsymbol{p}_2^2} + \hat{V}(r))]^{\frac{q_1}{1-q_1}} 4\pi r^2\,\mathrm{d}r\,\mathrm{d}^3\boldsymbol{p}_1\,\mathrm{d}^3\boldsymbol{p}_2.
\end{aligned} \tag{17}$$

For calculation convenience, we sum up the lower discrete energy levels of π and ρ, which are measured in experiments in the first and second terms in equation (17), and integrate nearly continuous higher energy levels in the third term. In first and second terms, the energy of π and ρ solved by TBDE [51] is $E_\pi = 0.159$ GeV and $E_\rho = 0.792$ GeV. In the third term, V is the motion volume of a π meson; we take V as the volume of the hadron gas, $V = \frac{4}{3}\pi r_0^3$, where r_0 is the radius of the hadron gas. $r_{\min}$ is the lower limit of the quark distance, with its value set as the lattice spacing for light quarks [57, 58] shown in table 1. $r_{\max}$ is the upper limit of quark distance; here, we set $r_{\max} = r_0$. $p_{\min} = 0.29$ GeV is the lower limit of quark momentum as the quark momentum at ρ state.

In the above, we have discussed the escort probability of a π meson while considering self-similarity structure based on the fractal theory. Tsallis entropy is associated with the escort probability in multifractals and follows the maximum entropy principle [56, 59, 60]. Meanwhile, entropy plays a crucial role in studying physical properties. In our model, we derive the Tsallis entropy of a $u\bar{d}$ bound system as

$$\begin{aligned}
S_{\pi 1} &= \frac{1 - \sum_{i=1}^{W} P_{1i}^{q_1}}{q_1 - 1} = \frac{1}{q_1 - 1} \\
&\quad \times \left\{1 - \frac{\sum_i \langle\psi_i\,|\,[1 + (q_1 - 1)\beta\hat{H}]^{\frac{q_1}{1-q_1}}\,|\,\psi_i\rangle}{\left\{\sum_i \langle\psi_i\,|\,[1 + (q_1 - 1)\beta\hat{H}]^{\frac{1}{1-q_1}}\,|\,\psi_i\rangle\right\}^{q_1}}\right\}.
\end{aligned} \tag{18}$$

Second, we analyze a π meson influenced by self-similarity structure in the quark aspect. We introduce the modification factor q_0 for self-similarity structure influence on

Table 1. The factors q_1 and q_2 in Au+Au collisions at $\sqrt{s_{\rm NN}}$ = 7.7, 11.5, 19.6, 27, 39 GeV for 0–5% centrality solved by TBFM.

$\sqrt{s_{\rm NN}}$/ GeV	T/ GeV	μ_B/GeV	$r_{\rm min}$/ fm	r_0/fm	q_1	q_2
7.7	0.1424 ± 0.00137	0.42	0.14	6.7	1.03062 ± 0.001100	1.13426 ± 0.004055
11.5	0.1483 ± 0.00142	0.316	0.12	6.7	1.03451 ± 0.002688	1.12593 ± 0.006648
19.6	0.1527 ± 0.00147	0.206	0.11	6.95	1.03595 ± 0.002156	1.11965 ± 0.006417
27	0.1541 ± 0.00148	0.156	0.11	6.95	1.04224 ± 0.002919	1.10896 ± 0.005396
39	0.155 ± 0.00149	0.112	0.11	7	1.04482 ± 0.001929	1.10500 ± 0.004225

u or $\bar{d}$ quarks, which comes from the influence of the strong interaction between u and $\bar{d}$ inside a π meson, and the influence of outside hadrons on pions. The probability of u, $\bar{d}$ quarks inside a π meson also obeys power-law form as

$$P_u = P_{\bar{d}} = \frac{\langle\phi_{q0}|[1+(q_0-1)\beta\hat{H}_q]^{\frac{q_0}{1-q_0}}|\phi_{q0}\rangle}{\sum_j\langle\phi_{qj}|[1+(q_0-1)\beta\hat{H}_q]^{\frac{q_0}{1-q_0}}|\phi_{qj}\rangle}, \quad (19)$$

where $\hat{H}_q$ is the Hamiltonian of the quark and the anti-quark with $\hat{H}_q = \hat{H}_{\bar{q}} = \sqrt{m_q^2+\boldsymbol{p}^2}$. ϕ_{q0} is the wavefunction of u, $\bar{d}$ quarks in the π state and ϕ_{qj} is the wavefunction of u, $\bar{d}$ quarks in different bound states.

The escort probability of a π meson can be expressed as the product of the escort probability of u and $\bar{d}$ quarks, $P_{\pi 2} = P_u \cdot P_{\bar{d}}$. Because of the pseudoadditivity [54] in non-extensive statistics, we define the escort parameter q_2 and it satisfies

$$\begin{aligned}&\langle\phi_j|[1+(q_2-1)\beta\hat{H}_t]^{\frac{q_2}{1-q_2}}|\phi_j\rangle\\ &\quad=\langle\phi_{qj}|[1+(q_0-1)\beta\hat{H}_q]^{\frac{q_0}{1-q_0}}|\phi_{qj}\rangle\\ &\quad\times\langle\phi_{qj}|[1+(q_0-1)\beta\hat{H}_q]^{\frac{q_0}{1-q_0}}|\phi_{qj}\rangle,\end{aligned} \quad (20)$$

where $\hat{H}_t = \sqrt{m_q^2+\boldsymbol{p_1}^2} + \sqrt{m_q^2+\boldsymbol{p_2}^2}$ and ϕ_j is the wavefunction of $u\bar{d}$ bound system.

So the escort probability of π meson is given by

$$P_{\pi 2} = P_u \cdot P_{\bar{d}} = \frac{\langle\phi_0|[1+(q_2-1)\beta\hat{H}_t]^{\frac{q_2}{1-q_2}}|\phi_0\rangle}{\sum_j\langle\phi_j|[1+(q_2-1)\beta\hat{H}_t]^{\frac{q_2}{1-q_2}}|\phi_j\rangle}, \quad (21)$$

where ϕ_0 is the wavefunction of the $u\bar{d}$ bound system in the π bound state. The denominator in equation (21) is the partition function for the quark and it sums up the probability of u, $\bar{d}$ quarks in all microstates as

$$\begin{aligned}&\sum_j\langle\phi_j|[1+(q_2-1)\beta\hat{H}_t]^{\frac{q_2}{1-q_2}}|\phi_j\rangle\\ &=[1+(q_2-1)\beta E_{u\bar{d}\pi}]^{\frac{q_2}{1-q_2}}+[1+(q_2-1)\beta E_{u\bar{d}\rho}]^{\frac{q_2}{1-q_2}}\\ &+\frac{V_q^2}{(2\pi)^6}\int_{p_{\rm min}}^{\infty}[1+(q_2-1)\beta\\ &\times(\sqrt{m_q^2+\boldsymbol{p_1}^2}+\sqrt{m_q^2+\boldsymbol{p_2}^2})]^{\frac{q_2}{1-q_2}}{\rm d}^3\boldsymbol{p_1}\,{\rm d}^3\boldsymbol{p_2},\end{aligned} \quad (22)$$

where $E_{u\bar{d}\pi}$, $E_{u\bar{d}\rho}$ represent the kinetic energy of quarks in the π and the ρ state, respectively, and they are calculated by the TBDE [51], $E_{u\bar{d}\pi} = 0.8508\,{\rm GeV}$, $E_{u\bar{d}\rho} = 0.3085\,{\rm GeV}$. V_q denotes the motion volume of u, $\bar{d}$ quarks, which approximately equals the motion volume of π meson V.

Meanwhile, the corresponding Tsallis entropy of the $u\bar{d}$ bound system is given by

$$\begin{aligned}S_{\pi 2} &= \frac{1-\sum_{j=1}^{W}P_{2j}^{q_2}}{q_2-1} = \frac{1}{q_2-1}\\ &\times\left\{1-\frac{\sum_j\langle\phi_j|[1+(q_2-1)\beta\hat{H}_t]^{\frac{q_2}{1-q_2}}|\phi_j\rangle}{\left\{\sum_j\langle\phi_j|[1+(q_2-1)\beta\hat{H}_t]^{\frac{1}{1-q_2}}|\phi_j\rangle\right\}^{q_2}}\right\}.\end{aligned} \quad (23)$$

Overall, we have analyzed the π meson from meson and quark aspects separately. From the meson aspect, the π meson satisfies self-similarity. By introducing the modification factor q_1, we obtain the probability of a π meson as in equation (14) and the entropy of a $u\bar{d}$ bound system as in equation (18). From the quark aspect, the u, $\bar{d}$ quarks also satisfy self-similarity. Their probabilities follow a power-law form, leading to the probability of a π meson being the product of the probabilities of u, $\bar{d}$ quarks. The escort parameter q_2 is applied to derive the probability of a π meson as in equation (21) and the entropy of a $u\bar{d}$ bound system as in equation (23). In fractal theory, the probabilities and Tsallis entropies for a π meson in the meson and the quark aspect should equal each other; thus,

$$P_{\pi 1} = P_{\pi 2}, \qquad S_{\pi 1} = S_{\pi 2}. \quad (24)$$

Considering different situations at different collision energies, the conservation equation sets (24) can be applied to evaluate the two-body self-similarity structure influence on pion gas at different collision energies. The parameter q_1 describes the self-similarity structure influence on the π meson in the meson aspect, and the escort parameter q_2 denotes the quark interaction in the π meson and the self-similarity structure influence on the π meson in the quark aspect.

To study the temperature evolution of modification factor q_1, we solve the equation sets (24) to obtain q_1 in Au+Au collisions at $\sqrt{s_{\rm NN}} = 39$ GeV. Shown in figure 4 is the modification factor q_1 at $\sqrt{s_{\rm NN}} = 39$ GeV. It is found that $q_1 > 1$, demonstrating that the similarity structure decreases the number of microstates. In the context of non-extensive statistics, if $q_1 > 1$, $S_q < S_{B-G}$. Moreover, it is found that q_1 decreases with decreasing temperature, so pion gas is

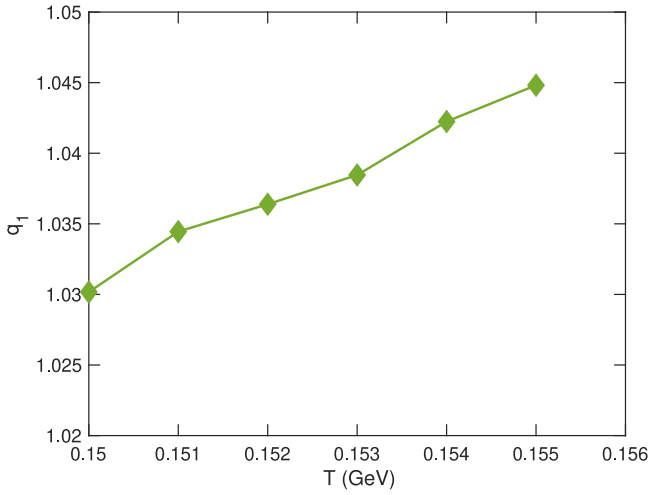

Figure 4. The relationship between the influence factor q_1 and the temperature T near to the critical temperature in Au+Au collisions at $\sqrt{s_{\rm NN}} = 39$ GeV.

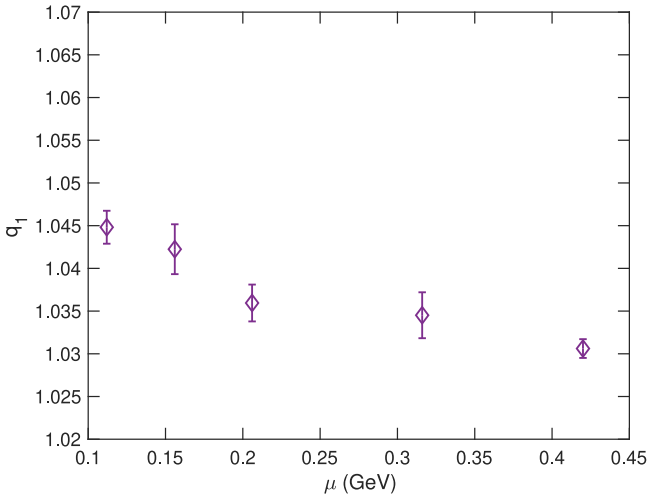

Figure 5. The relationship between modification factor q_1 and baryon chemical potential μ.

typically influenced by self-similarity structure near to the phase transition temperature.

From the lattice QCD phase diagram [8], we extract the temperature and the chemical potential of the phase transition within the range of error for different collision energies, which are listed in the second and third columns of table 1. Substituting the temperature and the radius of motion volumes, q_1 and q_2 can be solved in equation sets (24). Table 1 presents the parameters q_1 and q_2 solved for Au+Au collisions at $\sqrt{s_{\rm NN}} = 7.7$, 11.5, 19.6, 27, 39 GeV for 0–5% centrality. q_1 is larger than 1 at all collision energies, suggesting the existence of self-similarity structure. As the collision energy increases, the temperature of phase transition and the motion volume of π mesons increase and q_1 also becomes larger. This tendency suggests that the influence of $\pi - \pi$ self-similarity structure becomes stronger with the increase in collision energy. This is consistent with the collective flow effect being stronger at larger collision energies, leading to stronger resonance, so the self-similarity structure influence becomes stronger.

We analyze the values of chemical potential and self-similarity modification factor q_1, shown in figure 5, and find that with the decrease of the collision energy, the chemical potential μ increases, and the modification factor q_1 decreases. The variation of q_1 with μ follows a specific rule, as summarized in the parameter equation:

$$q_1 = 0.0393e^{-1.9342\mu} + 1.0132. \tag{25}$$

Based on this rule, in the planned collision energy region $\sqrt{s_{\rm NN}} = 2.2 \sim 4.5$ GeV in HIAF, we obtain $q_1 = 1.0208 \sim 1.0224$.

Regarding a $u\bar{d}$ bound system as a grand canonical ensemble and based on the escort probability of pion in equation (14), the normalized density operator $\hat{\rho}$ is expressed as [61]

$$\hat{\rho} = \frac{[1 + (q_1 - 1)\beta(\hat{H} - \mu\hat{N})]^{\frac{q_1}{(1-q_1)}}}{{\rm Tr}\,[1 + (q_1 - 1)\beta(\hat{H} - \mu\hat{N})]^{\frac{q_1}{(1-q_1)}}}, \tag{26}$$

where $\hat{N}$ denotes the particle number operator of the grand canonical ensemble.

Based on the density operator $\hat{\rho}$ and the pseudoadditivity law [62–64], the particle number distribution for a π meson can be obtained [33]:

$$\bar{n}_\pi = \frac{1}{[1 + (q_1 - 1)\beta(\varepsilon_\pi - \mu)]^{\frac{q_1}{(q_1-1)}} - 1}, \tag{27}$$

where ε_π is the energy of the π meson. In the limit $q_1 \to 1$, the distribution converges to become a Bose–Einstein distribution.

With the π meson distribution, the energy density u_π, pressure P_π and entropy density s_π can be calculated from the following formulas:

$$u_\pi = \frac{g_\pi}{2\pi^2}\int_0^\infty \varepsilon_\pi \bar{n}_\pi p_\pi^2 {\rm d}p_\pi, \tag{28}$$

$$P_\pi = \frac{\partial E}{\partial V} = \frac{g_\pi}{6\pi^2}\int_0^\infty \frac{p_\pi^4}{\varepsilon_\pi}\bar{n}_\pi {\rm d}p_\pi, \tag{29}$$

$$s_\pi = -\frac{g_\pi}{2\pi^2}\int_0^\infty [\bar{n}_\pi \ln \bar{n}_\pi - (1 + \bar{n}_\pi)\ln(1 + \bar{n}_\pi)]p_\pi^2 {\rm d}p_\pi, \tag{30}$$

where p_π is the momentum of the π meson. $g_\pi = 3$ is the degeneracy of the π meson and V is the volume of pion gas. The sign of pressure is defined as positive in the expanding direction.

We take $q_1 = 1.03595$, 1.04482 in Au+Au collisions at $\sqrt{s_{\rm NN}} = 19.6$, 39 GeV listed in table 1 as an example to study the influence of self-similarity structure, caused by resonance, quantum correlation and interaction, respectively. The self-similarity structure has most influence when

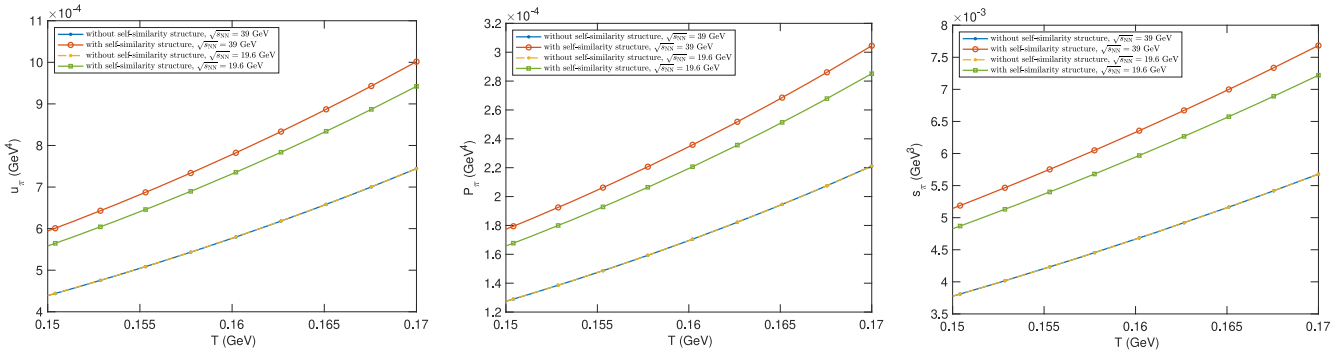

Figure 6. Thermodynamic quantities of pion gas with and without self-similarity structure influence in Au+Au collisions at $\sqrt{s_{\rm NN}} = 39, 19.6$ GeV.

approaching the transition temperature. We compare the quantities of pion gas with and without the influence of self-similarity structure just below the transition temperature as shown in figure 6. From figure 6, it can be found that the energy density, entropy density and pressure without the influence at $\sqrt{s_{\rm NN}} = 19.6, 39$ GeV are, respectively, the same. It is known that without the influence of self-similarity structure ($q = 1$), there is the same particle number distribution as the Bose–Einstein distribution at different collision energies, leading to the same physical properties. Shown in figure 6(a) is the energy density with and without self-similarity structure at $\sqrt{s_{\rm NN}} = 19.6, 39$ GeV collision energy. It can be seen that the energy density increases with the temperature. At fixed temperature for the same collision energy, the energy density under the influence of self-similarity is larger than that without the influence. This is because the interaction between two π mesons causes self-similarity structure, leading to the increase in energy density. At fixed temperature for different collision energies, the energy density under the influence of self-similarity structure at $\sqrt{s_{\rm NN}} = 39$ GeV (red trace) is larger than that at $\sqrt{s_{\rm NN}} = 19.6$ GeV (green trace), illustrating that there is stronger influence of self-similarity structure on pion gas at higher collision energy.

Shown in figure 6(b) is the pressure with and without self-similarity structure influence as a function of temperature. It can be seen that the pressure exhibits the same increasing trend as the energy density. This is because at fixed temperature the larger energy density under the influence of self-similarity structure induces larger pressure. Shown in figure 6(c) is the entropy density with and without self-similarity structure as a function of temperature. It shows that the entropy density increases with the temperature. At fixed temperature for the same collision, the entropy density with self-similarity structure influence is larger than without the influence. This is because the interaction potential between pions, one of the factors contributing to self-similarity structure, increases the microstates. Consequently, the entropy density increases. At fixed temperature for $\sqrt{s_{\rm NN}} = 19.6, 39$ GeV, with the influence of self-similarity structure, the entropy density at $\sqrt{s_{\rm NN}} = 39$ GeV (red trace) is larger than at $\sqrt{s_{\rm NN}} = 19.6$ GeV (green trace). It indicates a strengthened interaction between π mesons with increasing collision energy, leading to more two-body self-similarity structure. When the influence of self-similarity structure increases, the microstates increase and it also leads to the increase of entropy density.

With the particle number distribution of the π meson, in terms of the transverse momentum p_T and the rapidity y, we can derive the transverse momentum distribution function as

$$\frac{{\rm d}^2N}{2\pi p_T\,{\rm d}p_T\,{\rm d}y} = \frac{gV_{lab}m_T\cosh y}{(2\pi)^3} \times \frac{1}{[1+(q_1-1)\beta m_T\cosh y]^{\frac{q_1}{q_1-1}} - 1}, \quad (31)$$

where p_T is the transverse momentum in the lab frame, and $m_T = \sqrt{m^2 + p_T^2}$ is the transverse mass of the pion. V_{lab} is the motion volume of the π meson, related to the volume in center-of-mass frame V. The Lorentz transformation is $V_{lab} = \gamma V$, where γ is the Lorentz factor. In equation (31), q_1 can be solved through the TBFM in the meson aspect.

Substituting the value of q_1 from the TBFM into equation (31), we can derive the p_T spectrum of π mesons in Au+Au collisions at $\sqrt{s_{\rm NN}} = 7.7, 11.5, 19.6, 27, 39$ GeV for 0–5% centrality, and compare the results with experimental data shown in figure 7. In figure 7, the traces represent the transverse momentum distribution under the influence of the two-body self-similarity structure for pion gas produced in the collisions at $\sqrt{s_{\rm NN}} = 7.7, 11.5, 19.6, 27, 39$ GeV, and the colorful dots are the experimental transverse momentum distribution of these collisions. It can be seen that the theoretical results from the TBFM have good agreement with experimental data, illustrating that self-similarity structure exists in intermediate energy collisions, and influences the distribution of pion gas. If the distribution of pion gas is altered by the influence of self-similarity structure, the phase transition will also be impacted when considering the influence of self-similarity structure.

2.3. QCD phase diagram under the influence of QGP boundary effect and self-similarity structure of pions

In heavy-ion collisions, QGP undergoes a phase transition and turns into hadrons. As discussed above, the properties of

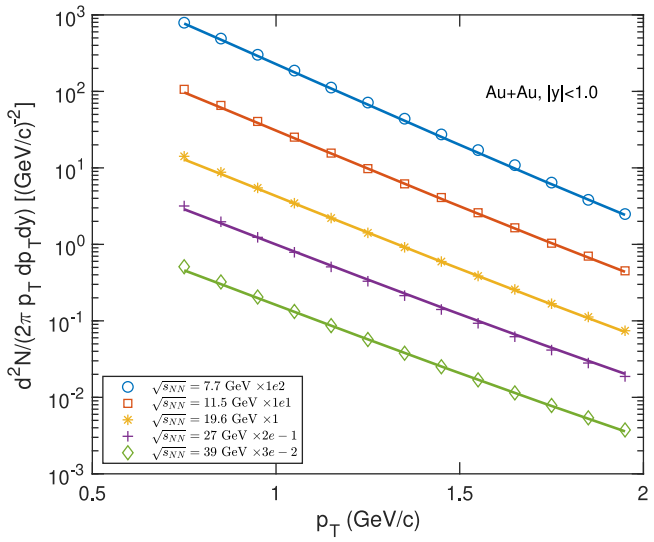

Figure 7. Transverse momentum spectra of π^+ meson in Au+Au collisions at $\sqrt{s_{\rm NN}} = 7.7, 11.5, 19.6, 27, 39$ GeV for 0–5% centrality, in mid-rapidity $|y| < 0.1$. The experimental data are from STAR [65].

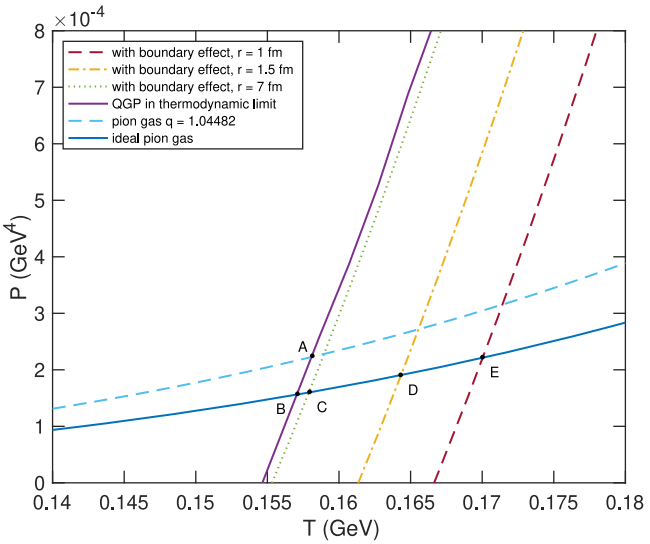

Figure 8. The pressure of the hadron phase in Au+Au collisions at $\sqrt{s_{\rm NN}} = 39$ GeV and that of QGP droplets at different radii, $r = 1, 1.5, 7$ fm.

QGP are influenced by the boundary effect, and those of hadrons are affected by self-similarity structure. The influence on two phases will surely impact the phase transition temperature. Based on the equilibrium condition that $T_{\rm QGP} = T_\pi$, $P_{\rm QGP} = P_\pi$, $\mu_{\rm QGP} = \mu_\pi$, with the QGP pressure in equation (12) and hadron pressure in equation (29), the phase transition temperature can be determined. Shown in figure 8 is the pressure of the QGP phase and the hadron phase in Au+Au collisions at $\sqrt{s_{\rm NN}} = 39$ GeV with baryon chemical potential $\mu = 0.112$GeV. The traces on the left side correspond to the pressure of the hadron phase, those on the right side correspond to the QGP phase, and the intersections correspond to the phase transition points. We also calculate the phase transition temperature at different fixed chemical potentials and different collision energies as shown in figure 9, which displays the phase diagrams from heavy-ion collisions.

In order to study the individual influence of the QGP boundary effect and self-similarity structure of pions, we firstly neglect self-similarity structure on pions and treat pions as an ideal gas through setting $q_1 = 1$ (blue solid trace) to study the QGP boundary effect. As shown in figure 8, the blue solid trace intersects with the trace of the pressure of QGP phase in the thermodynamic limit at point B, and intersects with these traces under the QGP boundary effect at QGP radii $r = 1, 1.5, 7$ fm at points C, D, E, respectively. It is observed that the phase transition temperature increases due to the boundary effect and follows the pattern $T_B < T_C < T_D < T_E$. This increase is attributed to the reduction of QGP pressure due to the boundary effect. In order to reach the phase transition pressure, the phase transition temperature should be increased. The smaller the QGP radius, the stronger the boundary effect, leading to a greater increase in the phase transition temperature.

We study not only the phase transition temperature at collision energy $\sqrt{s_{\rm NN}} = 39$ GeV and $\mu = 0.112$ GeV but

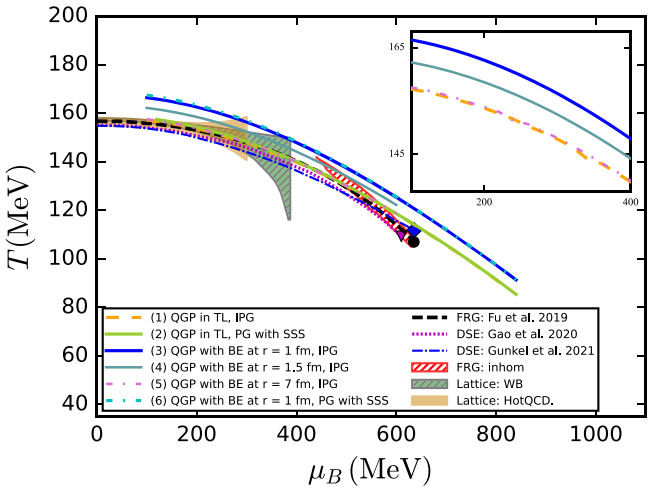

Figure 9. The phase diagram considering (1) QGP in the thermodynamic limit (TL) and ideal pion gas (IPG); (2) QGP in the thermodynamic limit and pion gas (PG) with the influence of self-similarity structure (SSS); (3), (4) and (5) QGP droplets with the boundary effect (BE) at different radii, $r = 1, 1.5, 7$ fm and ideal pion gas, respectively; (6) QGP droplet with the BE at radius $r = 1$ fm and pion gas with the influence of SSS. We also list the results from the functional renormalization group (fRG) model [66], Dyson–Schwinger equations (DSE) [67, 68] and lattice QCD [48, 49] for comparison.

also the temperature at different collision energies and different fixed baryon chemical potentials. As shown in figure 9, the blue solid trace, the cadet blue solid trace and the pink dotted trace correspond to the phase diagrams with QGP radius $r = 1, 1.5, 7$ fm, respectively. A detailed presentation of three traces is inset in the upper right part of figure 9. It can be seen that at different chemical potentials the trend of phase transition temperature under the influence of the boundary effect is the same as that in the $\sqrt{s_{\rm NN}} = 39$ GeV case, that is, $T_{PT,r=7\rm fm} < T_{PT,r=1.5\rm fm} < T_{PT,r=1\rm fm}$. This demonstrates that at different collision energies the boundary effect also increases

the transition temperature. The influence becomes more pronounced with decreasing QGP droplet radius.

Secondly, we consider QGP in the thermodynamic limit and focus on the self-similarity in the hadron phase to study the influence of resonance, interaction and quantum correlation on phase transition temperature. As shown in figure 8, the intersection A of the blue dashed trace in the hadron phase and the purple solid trace in the QGP phase corresponds to the phase transition point under the influence of self-similarity structure in the hadron phase. It can be seen that the phase transition temperature T_A under the influence of self-similarity structure is higher than without the influence, T_B. This is because self-similarity structure increases the pressure of the hadron phase. In order to have the two pressure traces in the two phases intersect, the phase transition pressure should be elevated, so that the phase transition temperature increases. We also compute the phase transition temperature under the influence of self-similarity structure in the hadron phase at different collision energies and different chemical potentials based on equation (25) and shown as the green solid trace in figure 9. It can be seen that this trace is slightly above the ideal gas (orange dashed trace) in the low and mid chemical potential region, suggesting that self-similarity structure increases the transition temperature in this region. In the high chemical potential region, the transition temperature is approximately the same as that for an ideal pion gas. This is consistent with the prediction of the TBFM discussed in section 2.2 that the influence of self-similarity structure decreases with increasing chemical potential. In the higher chemical potential region, the collision energy is smaller, leading to a smaller collective flow velocity, so that the resonance effect is smaller, and the influence of self-similarity structure diminishes correspondingly.

Lastly, we take the boundary effect of QGP droplets and the influence of two-body similarity structure on the pion gas both into account, and explore the phase transition in the intermediate and high baryon chemical potential region ($0.4 \sim 0.85$GeV), which could be produced in the future HIAF. In figure 9, the phase transition of QGP in the thermodynamic limit (orange dashed trace), the phase transition of QGP droplets at radius $r = 1$ fm with the boundary effect (blue solid trace) and the phase transition of QGP droplets with the boundary effect and the two-body similarity structure influence on pion gas (cyan dotted trace) are plotted. We also include the phase transition results from the fRG (functional renormalization group) approach [66], DSE (Dyson–Schwinger equations) model [67, 68] and lattice QCD [47, 48] in the finite chemical potential region for comparison.

As shown in figure 9, the cyan dotted trace (under the influence of the boundary effect in the QGP phase and self-similarity structure in the hadron phase) is a bit above the blue solid trace (only under the influence of the boundary effect in the QGP phase) in the low and mid chemical potential region, and approximately coincides with blue solid trace. The reason, explained above, is that the influence of self-similarity structure decreases with increasing chemical potential. It is also found that the cyan dotted trace is much higher than the green solid trace (only under the influence of self-similarity structure) and the orange dashed trace (QGP in the thermodynamic limit and pion ideal gas), indicating that the boundary effect with small QGP radius increases the phase transition temperature more than self-similarity structure in the hadron phase. This is because the pressure under the influence of the boundary effect in the QGP phase increases faster than that under the influence of self-similarity structure in the hadron phase. This faster increase in pressure under the influence of the boundary effect induces a larger increase in phase transition temperature.

3. Conclusion

We study the curved boundary effect on QGP droplets and the self-similarity structure effect on pion gas in intermediate- and low-energy heavy-ion collisions. In the QGP phase, we use the modified MIT bag model with the MRE method to study the boundary effect on QGP droplets. At fixed temperature, it is found that the energy density, entropy density and pressure with the boundary effect are smaller than those without this effect. The curvature of the boundary increases, leading to a greater decrease in the energy density, entropy density, and pressure.

In the hadron phase, we consider the resonance, strong interaction and quantum effects, which induce the self-similarity of the π–π two-meson state and the $u\bar{d}$ two-quark state of a pion. We develop a two-body fractal model (TBFM) to investigate the influence of self-similarity structure. In the framework of the TBFM, we introduce the modification factor q_1 to represent self-similarity structure influence on the π meson, and the escort parameter q_2 to characterize self-similarity structure influence on the quarks. We derive the probability and Tsallis entropy of the π meson from quark and meson aspects, and solve the corresponding equations to obtain the values of q_1 and q_2. The result $q_1 > 1$ suggests that the π gas is influenced by π–π two-body structures arising from resonance, interaction and quantum correlation effects. Furthermore, the value of q_1 decreases with decreasing temperature, prompting us to analyze self-similarity structure influence near the phase transition temperature. We simulate the temperature variation with chemical potential from lattice QCD and obtain q_1 as a function of chemical potential μ. It is found that q_1 decreases as the chemical potential increases. This is consistent with the trend where decreasing the collision energy and increasing the chemical potential lead to a decrease of the collective flow velocity, and subsequently decrease the influence of self-similarity structure. It is predicted that $q_1 = 1.0208 \sim 1.0224$ in the future HIAF energy region $\sqrt{s_{\rm NN}} = 2.2 \sim 4.5$ GeV. We compute the π meson distribution with self-similarity structure influence, and derive the energy density, entropy density and pressure of π mesons. It is found that the energy, entropy and pressure of π mesons increase compared to the results in the thermodynamic limit. Substituting q_1 into the non-extensive transverse momentum spectrum, it is observed to align well with the experimental data from Au+Au collisions at $\sqrt{s_{\rm NN}} = 7.7, 11.5, 19.6, 27, 39$ GeV.

Finally, we explore hadron–QGP phase transition under the influences of the boundary effect in QGP and two-body

self-similarity structure in pion gas. Considering the finite size QGP droplet, and utilizing the results of the TBFM in the intermediate chemical potential region, we derive the phase diagram with these effects, and compare the result to the phase diagram without these influences. Considering the boundary effect of QGP and treating the hadron phase as an ideal pion gas, we find that the phase transition temperature increases with the boundary effect. The smaller the QGP droplet and the stronger the boundary, the more the phase transition temperature increases. While considering QGP in the thermodynamic limit and pion gas influenced by the self-similarity structure, the phase transition temperature increases slightly with the influence at low and mid chemical potential, and remains approximately the same as that without the influence at high chemical potential. This suggests that there is smaller collective flow velocity in lower energy collisions, causing a smaller resonance effect and diminishing the influence of self-similarity structure. Considering both the boundary effect of QGP and the two-body self-similarity structure effect of pion gas, our analysis reveals that the phase transition temperature is higher compared to the temperature without the two effects, and increases slightly compared to that with only the boundary effect of QGP. This signifies the notable influence of the boundary effect and the surface tension in the high chemical potential region where the small QGP droplet can be produced. In contrast, the influence of self-similarity structure diminishes as the collective flow velocity decreases in this region. The result is instructive to future low-energy experiments that aim to observe the physics of the intermediate and high chemical potential region.

Acknowledgments

This work was supported by the National Natural Science Foundation of China under Grant No. 12175031, Guangdong Provincial Key Laboratory of Nuclear Science under Grant No. 2019B121203010.

References

[1] Singh C P 1993 Signals of quark-gluon plasma *Phys. Rep.* **236** 147
[2] Satz H 2000 Colour deconfinement in nuclear collisions *Rep. Prog. Phys.* **63** 1511
[3] Srivastava P K, Tiwari S K and Singh C P 2010 QCD critical point in a quasiparticle model *Phys. Rev.* D **82** 014023
[4] Arsene I and *et al.*(BRAHMS) 2005 Quark–gluon plasma and color glass condensate at RHIC? The perspective from the BRAHMS experiment *Nucl. Phys.* A **757** 1
[5] Back B B *et al* (PHOBOS) 2005 The PHOBOS perspective on discoveries at RHIC *Nucl. Phys.* A **757** 28
[6] Adams J *et al* (STAR) 2005 Experimental and theoretical challenges in the search for the quark-gluon Plasma: The STAR Collaboration's critical assessment of the evidence from RHIC collisions *Nucl. Phys.* A **757** 102
[7] Mohanty B 2009 QCD phase diagram: phase transition, critical point and fluctuations *Nucl. Phys.* A **830** 899
[8] An X *et al* 2022 The BEST framework for the search for the QCD critical point and the chiral magnetic effect *Nucl. Phys.* A **1017** 122343
[9] Karthein J M *et al* 2021 Strangeness-neutral equation of state for QCD with a critical point *Eur. Phys. J. Plus* **136** 621
[10] Odyniec G and (STAR) 2019 Beam Energy Scan Program at RHIC (BES I and BES II) - probing QCD phase diagram with heavy-ion collisions *PoS* **CORFU2018** 151
[11] Bzdak A, Esumi S, Koch V, Liao J-F, Stephanov M and Xu N 2020 Mapping the phases of quantum chromodynamics with beam energy scan *Phys. Rept.* **853** 1
[12] Li P-C *et al* 2023 Effects of a phase transition on two-pion interferometry in heavy ion collisions at $\sqrt{S_{NN}} = 2.4 - 7.7$ GeV *Sci. China Phys. Mech. Astron.* **66** 232011
[13] Luo X-F, Shi S-S, Xu N and Zhang Y F 2020 A study of the properties of the QCD phase diagram in high-energy nuclear collisions *Particles* **3** 278
[14] Bringoltz B and Teper M 2005 The pressure of the SU(N) lattice gauge theory at large *N Phys. Lett.* B **628** 113
[15] Callaway D J E and Rahman A 1982 Microcanonical ensemble formulation of lattice gauge theory *Phys. Rev. Lett.* **49** 613
[16] Geloun J B, Martini R and Oriti D 2016 Functional renormalization group analysis of tensorial group field theories on $\mathbb{R}^d$ *Phys. Rev.* D **94** 024017
[17] Aad G *et al* (ATLAS) 2010 Observation of a centrality-dependent dijet asymmetry in lead-lead collisions at $\sqrt{S_{NN}} = 2.76$ TeV with the ATLAS Detector at the LHC *Phys. Rev. Lett.* **105** 252303
[18] Kolb I, Horowitz W A and Mogliacci S 2019 Small system corrections to thermal field theory and pQCD energy loss *J. Phys.: Conf. Ser.* **1271** 012019
[19] Chatrchyan S *et al* (CMS) 2011 Observation and studies of jet quenching in PbPb collisions at $\sqrt{S_{NN}} = 2.76$ TeV *Phys. Rev.* C **84** 024906
[20] Aamodt K *et al* (ALICE) 2011 Suppression of charged particle production at large transverse momentum in central PbPb collisions at $\sqrt{S_{NN}} = 2.76$ TeV *Phys. Lett.* B **696** 30
[21] Venugopalan R and Prakash M 1992 Thermal properties of interacting hadrons *Nucl. Phys.* A **546** 718
[22] Deur A, Brodsky S J and de Tramond G F 2016 The QCD running coupling *Prog. Part. Nucl. Phys.* **90** 1
[23] Sahoo R 2019 Possible formation of QGP-droplets in proton-proton collisions at the CERN Large Hadron Collider *AAPPS Bull.* **29** 16
[24] Niida T and Miake Y 2021 Signatures of QGP at RHIC and the LHC *AAPPS Bull* **31** 12
[25] Loizides C 2016 Experimental overview on small collision systems at the LHC *Nucl. Phys.* A **956** 200
[26] Wong C-Y and Zhang W-N 2007 Single-event Handbury–Brown–Twiss interferometry *Int. J. Mod. Phys.* E **16** 3271
[27] Shneider M N and Pekker M 2019 Surface tension of small bubbles and droplets and the cavitation threshold arXiv:1901.04329
[28] Danielewicz P and Odyniec G 1985 Transverse momentum analysis of collective motion in relativistic nuclear collisions *Phys. Lett.* B **157** 146
[29] Gustafsson H A *et al* 1984 Collective flow observed in relativistic nuclear collisions *Phys. Rev. Lett.* **52** 1590
[30] Wiranata A, Koch V, Prakash M and Wang X-N 2014 Shear viscosity of a multi-component hadronic system *J. Phys.: Conf. Ser.* **509** 012049
[31] Zachariasen F and Zemach C 1962 Pion resonances *Phys. Rev.* **128** 849
[32] Hansson T H and Jaffe R L 1983 The multiple reflection expansion for confined scalar, Dirac, and gauge fields *Ann. Phys.* **151** 204
[33] Ding H-Q *et al* 2023 The spectrum of low-pT J/ψ in heavy-ion collisions in a statistical two-body fractal model *Entropy* **25** 1655

[34] Becattini B 2014 The quark gluon plasma and relativistic heavy ion collisions in the LHC era *J. Phys.: Conf. Ser.* **527** 012012
[35] Moreau P *et al* 2019 Exploring the partonic phase at finite chemical potential within an extended off-shell transport approach *Phys. Rev.* C **100** 014911
[36] Shen C and Alzhrani S 2020 Collision-geometry-based 3D initial condition for relativistic heavy-ion collisions *Phys. Rev.* C **102** 014909
[37] Adam J *et al* (STAR) 2020 Strange hadron production in Au +Au collisions at $\sqrt{S_{NN}}$ = 7.7, 11.5, 19.6, 27, and 39 GeV *Phys. Rev.* C **102** 034909
[38] Albacete J L, Guerrero-Rodrìguez P and Marquet C 2019 Initial correlations of the Glasma energy-momentum tensor *J. High Energy Phys.* **2019** 73
[39] Odyniec G 1999 Statistical and dynamical fluctuations in heavy ion collisions: role of conservation laws in event-by-event analysis *Acta Phys. Polon.* B **30** 385
[40] Chodos A, Jaffe R L, Johnson K, Thorn C B and Weisskopf V F 1974 New extended model of hadrons *Phys. Rev.* D **9** 3471
[41] Ramanathan R, Gupta K K, Jha A K and Singh S S 2007 The interfacial surface tension of a quark-gluon plasma fireball in a hadronic medium *Pramana* **68** 757
[42] Madsen J 1993 Curvature contribution to the mass of strangelets *Phys. Rev. Lett.* **70** 391
[43] Madsen J 1994 Shell model versus liquid drop model for strangelets *Phys. Rev.* D **50** 3328
[44] Balian R and Bloch C 1970 Distribution of eigenfrequencies for the wave equation in a finite domain *Ann. Phys.* **60** 401
[45] Jensen D M 2019 Strangelets-effects of finite size and exact color singletness arXiv:1904.04534
[46] Patra B K and Singh C P 1996 Temperature and baryon-chemical-potential-dependent bag pressure for a deconfining phase transition *Phys. Rev.* D **54** 3551
[47] Gao S, Wang E-K and Li J-R 1992 Bag constant and deconfinement phase transition in a nontopological soliton model *Phys. Rev.* D **46** 3211
[48] Bazavov A *et al* (HotQCD) 2019 Chiral crossover in QCD at zero and non-zero chemical potentials *Phys. Lett.* B **795** 15
[49] Bellwied R *et al* 2015 The QCD phase diagram from analytic continuation *Phys. Lett.* B **751** 559
[50] Hagedorn R 1973 Thermodynamics of strong interactions *Cargese Lect. Phys.* **6** 643
[51] Crater H W, Yoon J-H and Wong C-Y 2009 Singularity structures in Coulomb-type potentials in two-body Dirac equations of constraint dynamics *Phys. Rev.* D **79** 264
[52] Mandelbrot B B 1967 How long is the coast of Britain? Statistical self-similarity and fractional dimension *Science* **156** 636
[53] Mandelbrot B B 1986 Self-affine Fractal Sets, I: The Basic Fractal Dimensions *Fractals in Physics* (Amsterdam: Elsevier) 3–15
[54] Tsallis C 1988 Possible generalization of Boltzmann–Gibbs statistics *J. Stat. Phys* **52** 479
[55] Abe S and Okamoto Y 2001 *Nonextensive Statistical Mechanics and Its Applications* (vol 560) (Berlin: Springer)
[56] Tsallis C 2009 *Introduction to Nonextensive Statistical Mechanics: Approaching a Complex World* (vol 1) (New York: Springer)
[57] Feng X, Jin L-C and Riberdy M J 2022 Lattice QCD calculation of the pion mass splitting *Phys. Rev. Lett.* **128** 052003
[58] Wang G, Liang J, Draper T, Liu K-F and Yang Y-B 2021 Lattice calculation of pion form factors with overlap fermions *Phys. Rev.* D **104** 07452
[59] Ubriaco M R 1999 Thermodynamics of boson and fermion systems with fractal distribution functions *Phys. Rev.* E **60** 165
[60] Bykkili F and Demirham D 1993 A fractal approach to entropy and distribution functions *Phys. Lett.* A **181** 24
[61] Rajagopal A K, Mendes R S and Lenzi E K 1998 Quantum statistical mechanics for nonextensive systems: Prediction for possible experimental tests *Phys. Rev. Lett.* **80** 3907
[62] Abe S 2001 General pseudoadditivity of composable entropy prescribed by the existence of equilibrium *Phys. Rev.* E **63** 061105
[63] Wang Q A 2002 Quantum gas distribution prescribed by factorization hypothesis of probability *Chaos Solitons Fractals* **14** 765
[64] Beck C 2000 Non-extensive statistical mechanics and particle spectra in elementary interactions *Physica* A **286** 164
[65] Adamczyk L *et al* (STAR) 2017 Bulk properties of the medium produced in relativistic heavy-ion collisions from the beam energy scan program *Phys. Rev.* C **96** 044904
[66] Fu W-J, Pawlowski J M and Rennecke F 2020 QCD phase structure at finite temperature and density *Phys. Rev.* D **101** 054032
[67] Gao F and Pawlowski J M 2021 Chiral phase structure and critical end point in QCD *Phys. Lett.* B **820** 136584
[68] Gunkel P J and Fischer C S 2021 Locating the critical endpoint of QCD: Mesonic backcoupling effects *Phys. Rev.* D **104** 054022